Monthly Notices
of the
ROYAL ASTRONOMICAL SOCIETY

MNRAS **443,** 2695–2704 (2014) doi:10.1093/mnras/stu1343

A relationship between specific star formation rate and metallicity gradient within $z \sim 1$ galaxies from KMOS-HiZELS

John P. Stott,[1⋆] David Sobral,[2,3] A. M. Swinbank,[1] Ian Smail,[1] Richard Bower,[1] Philip N. Best,[4] Ray M. Sharples,[1] James E. Geach[5] and Jorryt Matthee[3]

[1]*Institute for Computational Cosmology, Durham University, South Road, Durham DH1 3LE, UK*
[2]*Centro de Astronomia e Astrofísica da Universidade de Lisboa, Observatório Astronómico de Lisboa, Tapada da Ajuda, P-1349-018 Lisboa, Portugal*
[3]*Leiden Observatory, Leiden University, PO Box 9513, NL-2300 RA Leiden, the Netherlands*
[4]*SUPA, Institute for Astronomy, Royal Observatory of Edinburgh, Blackford Hill, Edinburgh EH9 3HJ, UK*
[5]*Centre for Astrophysics Research, Science & Technology Research Institute, University of Hertfordshire, Hatfield, Hertfordshire AL10 9AB, UK*

Accepted 2014 July 3. Received 2014 July 1; in original form 2014 March 14

ABSTRACT

We have observed a sample of typical $z \sim 1$ star-forming galaxies, selected from the HiZELS survey, with the new *K*-band Multi-Object Spectrograph (KMOS) near-infrared, multi-integral field unit instrument on the Very Large Telescope (VLT), in order to obtain their dynamics and metallicity gradients. The majority of our galaxies have a metallicity gradient consistent with being flat or negative (i.e. higher metallicity cores than outskirts). Intriguingly, we find a trend between metallicity gradient and specific star formation rate (sSFR), such that galaxies with a high sSFR tend to have relatively metal poor centres, a result which is strengthened when combined with data sets from the literature. This result appears to explain the discrepancies reported between different high-redshift studies and varying claims for evolution. From a galaxy evolution perspective, the trend we see would mean that a galaxy's sSFR is governed by the amount of metal-poor gas that can be funnelled into its core, triggered either by merging or through efficient accretion. In fact, merging may play a significant role as it is the starburst galaxies at all epochs, which have the more positive metallicity gradients. Our results may help to explain the origin of the fundamental metallicity relation, in which galaxies at a fixed mass are observed to have lower metallicities at higher star formation rates, especially if the metallicity is measured in an aperture encompassing only the central regions of the galaxy. Finally, we note that this study demonstrates the power of KMOS as an efficient instrument for large-scale resolved galaxy surveys.

Key words: galaxies: abundances – galaxies: evolution – galaxies: kinematics and dynamics.

1 INTRODUCTION

The gas phase metallicity of a galaxy reflects the past star-forming activity and the history of both gas inflow and outflow of the system. Observations of galaxy metallicity and its dependence on mass can therefore be used to trace this history by comparing local samples (e.g. Tremonti et al. 2004; Kewley & Ellison 2008) to those at higher redshifts (e.g. Savaglio et al. 2005; Erb et al. 2006; Maiolino et al. 2008; Lamareille et al. 2009; Pérez-Montero et al. 2009; Yabe et al. 2012; Stott et al. 2013b; Zahid et al. 2013). The results of such studies have generally found a strong evolution in the gas phase metallicity, with galaxies being more metal poor at increasing redshift. However, this is perhaps because the observed high-redshift galaxies tend to be more highly star forming, as there is now evidence that galaxies are found to sit on a similar plane of mass, metallicity and star formation rate (SFR) in both the local and high-redshift Universe (Lara-López et al. 2010; Mannucci et al. 2010; Stott et al. 2013b).

As well as studying the individual and average metallicities within galaxy populations, more detailed observations that trace the variation of metallicity within galaxies can also be employed in order to understand their evolution. Due to the spatially resolved, high signal-to-noise spectral observations required, this has mainly been performed for relatively small galaxy samples in the local Universe. In the first comprehensive study, Searle (1971) measured the differences in line ratios, and therefore the implied chemical abundance, between different H II regions within the same galaxy. The

⋆ E-mail: j.p.stott@durham.ac.uk

key result of Searle (1971) and subsequent studies is that galaxies in the local Universe tend to have negative radial metallicity gradients, such that the stars and gas in the outer regions appear less metal rich than those in the centre (e.g. Shields 1974; McCall, Rybski & Shields 1985; Vila-Costas & Edmunds 1992; Zaritsky, Kennicutt & Huchra 1994; Garnett et al. 1997; van Zee et al. 1998; Bresolin, Kennicutt & Ryan-Weber 2012; Sánchez et al. 2012, 2014 and see the review by Henry & Worthey 1999). At high redshift, detailed observations become more challenging and the results more contradictory with some authors finding abundance gradients that are consistent with being flat or negative (Swinbank et al. 2012; Jones et al. 2013) and others seeing evidence for positive gradients (Cresci et al. 2010; Queyrel et al. 2012).

From a theoretical perspective, disc galaxies that follow inside-out growth tend to have initially steep negative abundance gradients which then flatten at later times (e.g. Marcon-Uchida, Matteucci & Costa 2010; Stinson et al. 2010; Gibson et al. 2013). Observational support for this has been claimed, as Jones et al. (2013) find a small subset of their $z = 2$ galaxies that possess significantly steeper negative abundance gradients than local galaxies. Simulations also show that merging events will rapidly flatten existing metallicity gradients of galaxies by inducing an inflow of metal-poor gas to their central regions (Rupke, Kewley & Barnes 2010a). This effect has been witnessed in observations of low-redshift interacting galaxies (Rupke, Kewley & Chien 2010b). There is also the possibility that so-called cold flows of metal-poor gas at high redshift could lead to lower central metallicities (e.g. Cresci et al. 2010), but there is some uncertainty as to how and where any inflowing material is deposited (Kereš et al. 2005; Dekel, Sari & Ceverino 2009).

In order to study abundance gradients at $z \sim 1$, we have observed a representative sample of star-forming galaxies with the *K*-band Multi-Object Spectrograph (KMOS), which is a near-infrared multiple integral field spectrograph (Sharples et al. 2013). These galaxies are drawn from our large (10 square degree) narrow-band (NB) Hα survey in SA22 using WIRcam/Canada–France–Hawaii Telescope (CFHT; CF-HiZELS; Sobral et al. in preparation; Sobral et al. 2013b; Matthee et al. 2014). Due to the depth achieved by our observations ($\sim$0.2 $L^*_{z=0.8}$), the majority of our targets are 'typical' galaxies at this epoch which will likely evolve into $\sim L^*$ (or SFR$*$) galaxies by $z = 0$. This survey builds on our previous Hα NB imaging of degree-sized areas in redshift slices at $z = 0.40$, 0.84, 1.47 and 2.23 from the High-z Emission line survey (HiZELS; Geach et al. 2008; Sobral et al. 2009, 2012, 2013a).

The KMOS observations were performed as part of the Science Verification (SV[1]) and focus on two relatively overdense regions of Hα emitters within SA22 field of the CF-HiZELS survey. These observations provide spatially resolved Hα and [N II] measurements which allow us to obtain resolved dynamics and metallicities. The dynamical results for the first region are presented in Sobral et al. (2013b). In this paper, we use the combined data set from both regions to investigate the chemical abundance gradients and the dynamical properties of the galaxies.

We use a cosmology with $\Omega_\Lambda = 0.73$, $\Omega_m = 0.27$ and $H_0 = 72$ km s^{-1} Mpc^{-1}. We note that 1 arcsec corresponds to 7.6 kpc at $z = 0.81$ (the median redshift of the galaxies presented in this paper). All quoted magnitudes are on the AB system and we use a Chabrier (2003) initial mass function (IMF) throughout.

[1] http://www.eso.org/sci/activities/vltsv/kmossv.html

2 SAMPLE AND DATA

Our targets are selected from a survey using the NB lowOH2 filter ($\lambda = 1187 \pm 5$ nm) on WIRCam / CFHT (Puget et al. 2004), which covers a 10 deg^2 contiguous area in SA22 (Sobral et al. 2013b; Sobral et al. in preparation). The survey yields $\sim$3000 robust Hα emitters at $z = 0.81 \pm 0.01$ (see Sobral et al. 2013a and Sobral et al. in preparation for details on the spectroscopic and photometric redshifts, and colour–colour selection). We use the wealth of ancillary data, including seven-band photometric coverage [from *u* to *K* band, available in this field from the CFHT Legacy Survey (CFHTLS) and the United Kingdom Infrared Telescope Infrared Deep Sky Survey (UKIDSS)] to compute stellar masses for all of the Hα emitters in the parent sample following Sobral et al. (2011, 2014). The two regions that we target with KMOS are at RA $22^h19^m30\overset{s}{.}3$, Dec. $+00^\circ\ 38'\ 59''$ and RA $22^h19^m41\overset{s}{.}5$, Dec. $+00^\circ\ 23'\ 20''$ (J2000). Both of these observations were taken as part of the KMOS SV, and so we label the two fields KMOS-HiZELS-SV1 (see also Sobral et al. 2013b) and KMOS-HiZELS-SV2 (this paper), respectively.

The KMOS spectrograph consists of 24 integral field units (IFUs) that patrol a 7.2 arcmin field. Each IFU has an area of 2.8 arcsec $\times$ 2.8 arcsec with 0.2 arcsec $\times$ 0.2 arcsec spatial pixels. We identified target Hα emitters with NB Hα fluxes brighter than 1×10^{-16} erg s^{-1} cm^{-2}, (SFRs > 3.5 M$_\odot$ yr^{-1}, assuming 1 mag of extinction, Kennicutt 1998 and a Chabrier 2003 IMF) which lie within 7 arcmin diameter regions centred on KMOS-HiZELS-SV1 and KMOS-HiZELS-SV2. For KMOS-HiZELS-SV1, we selected the 21 of these galaxies which were brighter than $K_{AB} \sim 21.5$ (roughly corresponding to stellar mass $M_* > 10^{9.75}$ M$_\odot$). KMOS-HiZELS-SV2 has a lower number density of HiZELS sources and so we selected 12 Hα emitters and a further 9 galaxies with spectroscopic redshifts in the range $0.8 < z < 1.0$ from the VIMOS/VLT Deep Survey (VVDS) survey (Le Fèvre et al. 2005). We therefore selected 42 galaxies for observations during SV time with KMOS (although only 39 were observed due to technical problems, see below). The galaxies in this KMOS sample have a median stellar mass of $\sim 10^{10.1}$ M$_\odot$ yr^{-1}, a median SFR of 7 M$_\odot$ yr^{-1} and a median specific star formation rate (sSFR, SFR/M_*) of 0.5 Gyr^{-1} (see Fig. 1). Our KMOS sources are typical star-forming galaxies at their redshift [2–14 M$_\odot$ yr^{-1}, while the characteristic SFR (SFR$*$) at $z \sim 0.8$ is $\sim$8 M$_\odot$ yr^{-1}; cf. Sobral et al. 2014.

KMOS observations were taken in 2013 on June 29, July 1 (KMOS-HiZELS-SV1) and September 25 (KMOS-HiZELS-SV2). During the observations, the average *J*-band seeing was approximately 0.7 arcsec. We used the *YJ*-band grating in order to cover the Hα emission, which at $z \sim 0.81$ (CF-HiZELS NB) is redshifted to $\sim$1.187 μm. In this configuration, the spectral resolution is $R = \lambda / \Delta\lambda \sim 3400$. We also deployed three IFUs (one per KMOS spectrograph) to (blank) sky positions to improve the sky subtraction during the data reduction. Observations were carried out using an ABA (object-sky-object) sequence, with 450 s integration per position, in which we chopped by 5 arcsec to sky, and each observation was dithered by up to 0.2 arcsec. The total on-source integration time was 1.25 h per galaxy. During the KMOS-HiZELS-SV1 observations, three of the IFUs were disabled and so only 18 galaxies were observed in this pointing making 39 in total.

To reduce the data, we used the ESOREX/SPARK pipeline (Davies et al. 2013), which extracts the slices from each IFU, flat-fields and wavelength calibrates the data to form a data cube. We reduced each AB pair separately and improved the sky OH subtraction in each AB pair for each IFU using the data from the sky IFU from the appropriate spectrograph (using the sky-subtraction techniques

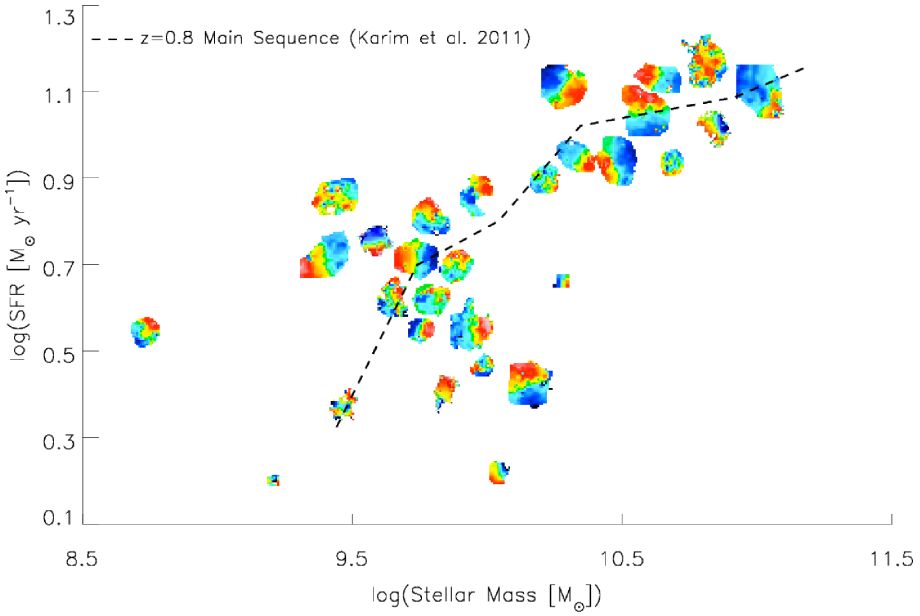

Figure 1. The SFR plotted against stellar mass for the 29 resolved galaxies in the KMOS-HiZELS sample with the data points represented by their velocity fields (normalized to their maximum observed velocities to make the rotation visible for a range of rotation speeds). For the velocity fields, red denotes a positive (recessional) velocity relative to the systemic redshift (green), while blue is negative. Note that positions are approximate to avoid galaxy velocity fields from overlapping. The dashed line represents the location of the 'main sequence' of star-forming galaxies at $z = 0.8$–1.0 from Karim et al. (2011), demonstrating that our sample is typical for this epoch.

described in Davies 2007). We then combined the data into the final data cube using a clipped average. We note that both the effects of instrumental resolution and the spatial point spread function are taken into account throughout the analysis and included in the error estimation.

For the KMOS-HiZELS-SV2 observations, 2 of the 21 galaxies observed returned no evidence of an emission line and a further six did not have resolved Hα emission (three of which came from the VVDS selection rather than the CF-HiZELS NB). For the remainder of this paper, we concentrate on the 29 resolved galaxies from the two KMOS-HiZELS pointings.

3 ANALYSIS AND RESULTS

3.1 Dynamics

We begin by determining the dynamical properties of the KMOS-HiZELS galaxies via disc model fitting and kinemetry before studying their resolved metallicities (see also Sobral et al. 2013b).

We collapse each reduced data cube into a one-dimensional spectrum and measure the redshift by fitting a Gaussian profile to the Hα and [N II] emission lines, for which we also recover their total flux. To measure the Hα dynamics of each galaxy, we fit the Hα and [N II] emission lines spaxel to spaxel using a χ^2 minimization procedure (accounting for the increased noise at the positions of the sky lines). We initially try to identify the Hα line in a 0.4 arcsec $\times$ 0.4 arcsec region (~ 3 kpc), and if the fit fails to detect the line with a signal-to-noise >5, the region is increased to 0.6 arcsec $\times$ 0.6 arcsec. When this criterion is met, the Hα and [N II] emission lines are fitted allowing the centroid, intensity and width of the Gaussian profile to find their optimum values [the full width at half-maxima (FWHM) of the Hα and [N II] lines are coupled in the fit]. Uncertainties are then calculated by perturbing each parameter, one at a time, allowing the remaining parameters to find their optimum values, until $\Delta\chi^2 = 1$ is reached.

The measured velocity fields for the resolved KMOS-HiZELS galaxies are displayed in Fig. 1 at the approximate positions of their stellar mass and SFR. Fig. 1 is therefore a plot of the so-called star-forming 'main sequence' (Noeske et al. 2007), with the points represented by the galaxy velocity fields. The position of the star-forming main sequence at $z = 0.8$-1 from Karim et al. (2011) is included, demonstrating that these galaxies are typical star-forming systems at this epoch. The majority of the galaxies display velocity gradients in their dynamics, with observed peak-to-peak differences ranging within $\Delta v \sim 40$–300 km s^{-1}.

Many of these galaxies have Hα velocity fields which resemble rotating systems (characteristic 'spider' patterns in the velocity fields and line-of-sight velocity dispersion profiles which peak near the central regions). Therefore, we attempt to model the two-dimensional velocity field to identify the dynamical centre and kinematic major axis. We follow Swinbank et al. (2012) to construct two-dimensional models with an input rotation curve following an arctan function [$v(r) = \frac{2}{\pi}\, v_{\rm asym}\, \arctan(r/r_{\rm t})$], where $v_{\rm asym}$ is the asymptotic rotational velocity and $r_{\rm t}$ is the effective radius at which the rotation curve turns over (Courteau 1997). The suite of two-dimensional models which we fit to the data have six free parameters [(x,y) centre, position angle, $r_{\rm t}$, $v_{\rm asym}$ and disc inclination], and we use a genetic algorithm (Charbonneau 1995) to find the best model (see Swinbank et al. 2012).

The best-fitting dynamical model produces a dynamical centre and position angle of the disc allowing us to extract the one-dimensional rotation curve and velocity dispersion profiles from the major kinematic axis of each galaxy. Despite the relatively short integration time (1.25 h on source), the data yield clear rotation curves which turn over (or flatten) for at least 10 of these galaxies (see also Sobral et al. 2013b).

Table 1. The details of the KMOS-HiZELS sample. The CF-HiZELS galaxies are named CFHT-NBJ, and the VVDS galaxies are numbered by our own internal catalogue system. The v_{80} parameter is the inclination corrected rotation speed at r_{80} ($r_{80} = 2.2r_e$). The KMOS-HiZELS-SV1 sample data are presented in Sobral et al. (2013b), and should be cited as such, but are included here below the horizontal line for completeness.

Galaxy	RA [J2000]	Dec. [J2000]	z	K_{AB}	r_e (kpc)	[N II]/Hα	log (M_*) ($M_\odot$)	SFR ($M_\odot$ yr^{-1})	v_{80} (km s^{-1})	K_{Tot}
CFHT-NBJ-C339	22:19:46.96	+00:25:02.5	0.8135	20.12	3.0	1.28 ± 0.12	10.6 ± 0.1	11.0	146.0	0.5 ± 0.5
CFHT-NBJ-C343	22:19:48.65	+00:21:28.4	0.8100	20.85	4.7	0.32 ± 0.13	10.5 ± 0.2	4.1	224.0	0.3 ± 0.1
CFHT-NBJ-956	22:19:27.05	+00:23:42.4	0.8095	21.43	4.5	0.15 ± 0.28	10.1 ± 0.2	4.1	231.0	0.2 ± 0.1
CFHT-NBJ-1209	22:19:40.16	+00:22:38.5	0.8085	21.76	10.4	0.13 ± 0.41	9.4 ± 0.1	5.4	219.0	0.1 ± 0.7
CFHT-NBJ-1478	22:19:41.06	+00:22:34.2	0.8105	22.10	3.9	0.18 ± 0.27	9.9 ± 0.4	4.6	148.0	5.1 ± 0.2
CFHT-NBJ-2044	22:19:34.37	+00:23:00.4	0.8099	19.67	8.3	0.59 ± 0.16	11.0 ± 0.1	12.5	260.0	0.2 ± 0.1
CFHT-NBJ-2048	22:19:51.67	+00:21:00.9	0.8155	22.90	5.8	0.11 ± 0.36	8.8 ± 0.1	3.5	89.0	0.3 ± 1.1
VVDS-432	22:19:46.70	+00:21:35.4	0.8095	21.24	4.8	0.17 ± 0.53	10.1 ± 0.2	1.2	144.0	–
VVDS-503	22:19:51.16	+00:25:42.2	0.9925	21.82	4.2	0.19 ± 0.21	9.4 ± 0.1	7.6	62.0	–
VVDS-588	22:19:32.41	+00:21:01.0	0.8770	20.90	2.2	0.54 ± 0.19	10.1 ± 0.1	2.2	207.0	0.5 ± 0.7
VVDS-888	22:19:38.00	+00:20:07.4	0.8331	22.10	1.3	0.27 ± 0.15	9.7 ± 0.1	4.6	56.0	0.4 ± 9.2
VVDS-942	22:19:39.44	+00:25:29.3	0.8095	23.41	4.0	–	9.2 ± 0.4	1.6	132.0	–
VVDS-944	22:19:39.73	+00:24:02.4	0.8970	22.31	2.1	–	9.5 ± 0.2	2.3	258.0	0.9 ± 0.3
KMOS-HiZELS-SV1, from Sobral et al. (2013b)										
CFHT-NBJ-1709	22:19:31.92	+00:36:11.6	0.8133	21.3	2.1	0.42 ± 0.06	10.7 ± 0.1	8.5	55.0	0.5 ± 0.10
CFHT-NBJ-1713	22:19:21.34	+00:36:42.7	0.7639	21.1	3.9	–	10.0 ± 0.2	7.4	–	–
CFHT-NBJ-1721	22:19:24.10	+00:37:11.2	0.8144	20.0	5.1	0.62 ± 0.06	10.8 ± 0.1	13.9	240.0	0.6 ± 0.2
CFHT-NBJ-1724	22:19:27.27	+00:37:31.3	0.8117	21.4	4.7	0.36 ± 0.08	10.1 ± 0.1	4.3	–	–
CFHT-NBJ-1733	22:19:43.57	+00:38:22.1	0.7731	22.2	3.8	0.19 ± 0.03	9.7 ± 0.3	7.6	90.0	1.4 ± 0.5
CFHT-NBJ-1739	22:19:42.27	+00:38:31.6	0.8042	20.1	6.0	0.40 ± 0.05	10.6 ± 0.2	11.4	247.0	0.5 ± 0.1
CFHT-NBJ-1740	22:19:18.60	+00:38:43.9	0.8128	21.2	5.0	0.32 ± 0.05	10.4 ± 0.1	8.9	217.0	0.3 ± 0.1
CFHT-NBJ-1745	22:19:29.51	+00:38:52.1	0.8174	22.0	4.1	0.16 ± 0.02	9.8 ± 0.3	5.6	211.0	0.2 ± 0.1
CFHT-NBJ-1759	22:19:41.42	+00:39:25.4	0.8035	20.3	4.1	0.39 ± 0.03	10.3 ± 0.2	12.9	275.0	0.2 ± 0.1
CFHT-NBJ-1770	22:19:27.66	+00:40:14.3	0.7731	21.7	3.9	0.05 ± 0.01	9.9 ± 0.3	10.4	144.0	0.4 ± 0.2
CFHT-NBJ-1774	22:19:30.59	+00:40:31.5	0.8127	21.7	3.8	0.19 ± 0.03	9.8 ± 0.2	4.2	50.0	0.3 ± 0.1
CFHT-NBJ-1787	22:19:39.21	+00:41:20.8	0.8132	20.5	6.5	0.41 ± 0.04	10.6 ± 0.2	12.0	255.0	0.3 ± 0.1
CFHT-NBJ-1789	22:19:23.19	+00:41:23.8	0.8130	20.6	9.5	0.32 ± 0.02	10.6 ± 0.1	11.8	253.0	0.1 ± 0.1
CFHT-NBJ-1790	22:19:24.69	+00:41:26.1	0.8124	22.0	1.7	0.30 ± 0.05	9.9 ± 0.3	4.7	30.0	0.4 ± 0.2
CFHT-NBJ-1793	22:19:30.60	+00:41:35.1	0.8161	21.3	9.3	0.30 ± 0.04	10.2 ± 0.2	7.8	–	–
CFHT-NBJ-1795	22:19:32.44	+00:41:42.3	0.8095	21.5	3.0	0.32 ± 0.04	9.8 ± 0.2	6.5	53.0	0.5 ± 0.1

We also measure the effective radii (r_e) of the KMOS-HiZELS sample by fitting a two-dimensional Sérsic profile to UKIDSS K-band images of the galaxies using the GALFIT (version 3) software package (Peng et al. 2002). This software requires reasonable initial input parameters such as position, apparent magnitude and ellipticity, all of which are estimated by first running the SExtractor package (Bertin & Arnouts 1996) so that the iterative fitting process converges to the correct solution in the shortest possible time. GALFIT deconvolves the atmospheric seeing for this ground-based imaging.

As discussed in Section 1, it is likely that merging events and/or cold flows may affect the metallicity gradient of galaxies by transporting gas of differing abundances throughout the disc (Cresci et al. 2009; Rupke et al. 2010a). In order to study the presence of mergers in our sample, we perform further analysis, to distinguish between a galaxy with dynamics dominated by ordered rotation or by disturbed kinematics via a method known as 'kinemetry'. Kinemetry measures the asymmetry of the velocity field and spatially resolved line-of-sight velocity dispersion for each galaxy. This method has been well calibrated and tested at low redshift (e.g. Krajnović et al. 2006), and used at high redshift to determine the strength of deviations of the observed velocity and dispersion maps from an ideal rotating disc (Shapiro et al. 2008; Swinbank et al. 2012; Sobral et al. 2013b; but see also Gonçalves et al. 2010). Briefly, in this modelling, the velocity and velocity dispersion maps are described by a series of concentric ellipses of increasing semi-major axis length, as defined by the system centre, position angle and inclination. Along each ellipse, the moment map as a function of angle is extracted and decomposed into its Fourier series which have coefficients k_n at each radii (see Krajnović et al. 2006 for more details).

We measure the velocity field and velocity dispersion asymmetry (K_V and K_σ, respectively) for all of the galaxies in our sample. For an ideal disc, the values of K_V and K_σ will be zero. In contrast, in a merging system, strong deviations from the idealized case cause large values of K_V and K_σ (which can reach $K_V \sim K_\sigma \sim 10$ for very disturbed systems). The total asymmetry, K_{Tot}, is $K_{Tot}^2 = K_V^2 + K_\sigma^2$. The majority of our sample have $K_{Tot} \lesssim 0.5$ and are therefore consistent with being rotation-dominated discs, despite residing in a relatively overdense region, which may in general lead to an increased merger rate. The number of galaxies with $K_{Tot} > 0.5$ is 4, which is consistent with the 10 per cent merger fraction found on the main sequence at $z \sim 0.8$ by Stott et al. (2013a). The dynamical properties of the KMOS-HiZELS sample are given in Table 1.

3.2 Metallicity gradients

We derive the metal content of our galaxies using emission line ratios. The gas phase abundance of oxygen [12 + log(O/H)] for the sample can be estimated from the ratio of the [N II] to Hα lines (Alloin et al. 1979; Denicoló, Terlevich & Terlevich 2002;

Kewley & Dopita 2002). This is often referred to as the N2 method, where

$$\mathrm{N2} = \log(f_{[\mathrm{N\,II}]}/f_{\mathrm{H}_\alpha}). \quad (1)$$

To convert from N2 to oxygen abundance, we use the conversion of Pettini & Pagel (2004), which is appropriate for high-redshift star-forming galaxies, where

$$12 + \log(\mathrm{O/H}) = 8.9 + 0.57\ \mathrm{N2}. \quad (2)$$

We first derived metallicities within an aperture of diameter 1.2 arcsec for comparison with our Subaru Fiber Multi Object Spectrograph (FMOS) study of HiZELS galaxy metallicities (Stott et al. 2013b). The median metallicity of the sample is $12 + \log(\mathrm{O/H}) = 8.63 \pm 0.11$, consistent with the solar value of 8.66 ± 0.05 (Asplund et al. 2004). In Table 1, we show the uncertainty in the [N II]-to-Hα ratio derived from the errors of the line profile fitting; however, we note that the Pettini & Pagel (2004) metallicity calibration has a 1σ scatter of 0.18 dex. The mass–metallicity relation for the KMOS-HiZELS galaxies is in agreement with both the low-redshift SDSS study of Tremonti et al. (2004) and the $z \sim 0.8$-1.5 relation displayed in Stott et al. (2013b) and is therefore consistent with no chemical abundance evolution since $z \sim 1$ (this is discussed in Stott et al. 2013b). In terms of active galactic nucleus (AGN) contamination, only one of the galaxies in the entire sample has N2 > 0.0 (CFHT-NBJ-C339) which may indicate that it is an AGN (Kewley et al. 2001).

To derive the metallicity gradients of the galaxies in our sample, we extract the average metallicity within elliptical annuli at increasing galactocentric radii. The ellipticity of these annuli is derived from the inclination angle of the best-fitting dynamical disc model, found in Section 3.1. The typical seeing for the observations is 0.7 arcsec which corresponds to ∼5 kpc. Given this, we choose to measure the metallicities in galactocentric annuli encompassing the radii: <3, 3–6 and 6–9 kpc (a discussion of the effects of seeing and inclination angle is provided in Section 3.2.1). In order to do this, we first subtract the velocity field of the best-fitting dynamical disc model, found in Section 3.1, from the data cube so that the Hα and [N II] emission lines are not broadened or superimposed. We then sum the IFU spectra in each of these annuli and fit the Hα 6563 and [N II] 6583 Å emission lines in the resulting 1D spectra with single Gaussian profiles in order to extract their total flux. For a detection, we enforce 5σ and 2σ detection thresholds over the continuum level for Hα and [N II], respectively (following Stott et al. 2013b). Examples of the spectra in each annulus for five galaxies from our sample are displayed in Fig. 2. To calculate the metallicity gradient, we use a χ^2 minimization to fit a straight line to the metallicity as a function of galactocentric radius and present the gradient values in Table 2. The metallicity gradient fits are also displayed in Fig. 2 with the radius normalized to the effective radius of the galaxy for ease of comparison. In total, we were able to extract metallicity gradients for 20 of the KMOS-HiZELS galaxies as the remainder had integrated [N II] lines which were either too low signal-to-noise or affected by the sky emission spectra. The measured metallicity gradient values are robust to the inclusion of the error arising from the 0.18 dex scatter in the Pettini & Pagel (2004) metallicity calibration, although this would increase the typical gradient errors quoted in Table 2 by a factor of $\gtrsim$2.

There is no evidence for the central annuli of any galaxy being dominated by AGN contamination except for the potential AGN CFHT-NBJ-C339 identified above. This galaxy has a high central N2 value of 0.1, although we note that it has a line ratio gradient consistent with being flat so there is no central concentration. However, the presence of unaccounted for AGN may act to boost the central N2 values of our galaxies, with both Wright et al. (2010) and Newman et al. (2014) finding that at $z > 1$ the region of the BPT (Baldwin, Phillips & Terlevich) diagram (Baldwin, Phillips & Terlevich 1981) at the boundary between star-forming galaxies and AGN contains some composite systems with spatially concentrated AGN imbedded within a star-forming galaxy. We do not have the Hβ and [O III] line diagnostics available to perform a BPT diagram. However, if we assume that some fraction of our sample may be affected by hidden AGN, then this would act to raise their central metallicities, steepening the negative metallicity gradients but flattening the positive ones. A further source of uncertainty is shock-excited gas due to winds, which could increase the N2 values at large galactic radii, acting on the measured metallicity gradients in the opposite sense to AGN contamination (Rich et al. 2010).

The average value of the metallicity gradient for our sample is $\frac{\Delta Z}{\Delta r} = -0.002 \pm 0.007$ dex kpc^{-1}. There are seven galaxies with a $>2\sigma$ significance of having a non-zero metallicity gradient with five of these having negative gradients and two positive.

We look for correlations between the metallicity gradient and the global properties of the galaxies. In Fig. 3, we plot the metallicity gradient against stellar mass and also include $z \sim$ 1–2 data points from the literature (Queyrel et al. 2012; Swinbank et al. 2012; Jones et al. 2013), who all use the Pettini & Pagel (2004) N2 method to determine their metallicities. The stellar masses of the literature data are all estimated with a Chabrier (2003) IMF (as are the KMOS-HiZELS masses) except for Queyrel et al. (2012), which for consistency we correct from a Salpeter (1955) IMF by dividing by a factor of 1.8. We note that the Jones et al. (2013) data are for gravitationally lensed galaxies, and therefore the metallicity gradients may be subject to the uncertainties in reconstructing the galaxy images, although they have the advantage of being at high spatial resolution. We perform an outlier-resistant linear regression to the combined high-redshift sample of KMOS-HiZELS, Queyrel et al. (2012), Jones et al. (2013) and Swinbank et al. (2012), which has the form $\frac{\Delta Z}{\Delta r} = a\ \log(M_\star) + b$, where $a = -0.022 \pm 0.009$ and $b = 0.22 \pm 0.03$ (i.e. the slope is 2.4σ from being flat). No significant correlations are found between metallicity gradient and SFR or effective radius, although we note that in the local Universe Sánchez et al. (2014) do find a correlation with radius.

From a simple physical perspective, we might also expect a trend between metallicity gradient and the kinemetry parameter, K_{Tot}, as this is a measure of how disturbed the system is, or sSFR, as this is a measure of how intensely the galaxy is forming stars, both of which will be associated with the motion of gas within the galaxy. Interestingly, we find no trend with K_{Tot} for our sample, but this is perhaps not surprising as the galaxies are selected to be typical of $z \sim 1$ star-forming galaxies, for which the incidence of mergers is only ∼10 per cent (Stott et al. 2013a), and probe only a small range in K_{Tot}. If we combine our data with the K_{Tot} values measured in Swinbank et al. (2012), there is still no trend, but again these are typical galaxies mainly in the $K_{\mathrm{Tot}} < 0.5$ regime. Unfortunately, we do not have the K_{Tot} values for the rest of the literature data.

Also displayed in Fig. 3 is the metallicity gradient plotted against sSFR for which we do see a trend, which is strengthened when our data are combined with those of Queyrel et al. (2012), Jones et al. (2013) and Swinbank et al. (2012). As above, we perform a fit to this combined high-redshift sample, which has the form $\frac{\Delta Z}{\Delta r} = c\ \log(\mathrm{sSFR}) + d$, where $c = 0.020 \pm 0.007$ and $d = 0.18 \pm 0.07$ (i.e. the slope is 2.9σ from being flat). We note that the two Jones et al. (2013) galaxies not shown in Fig. 3 are

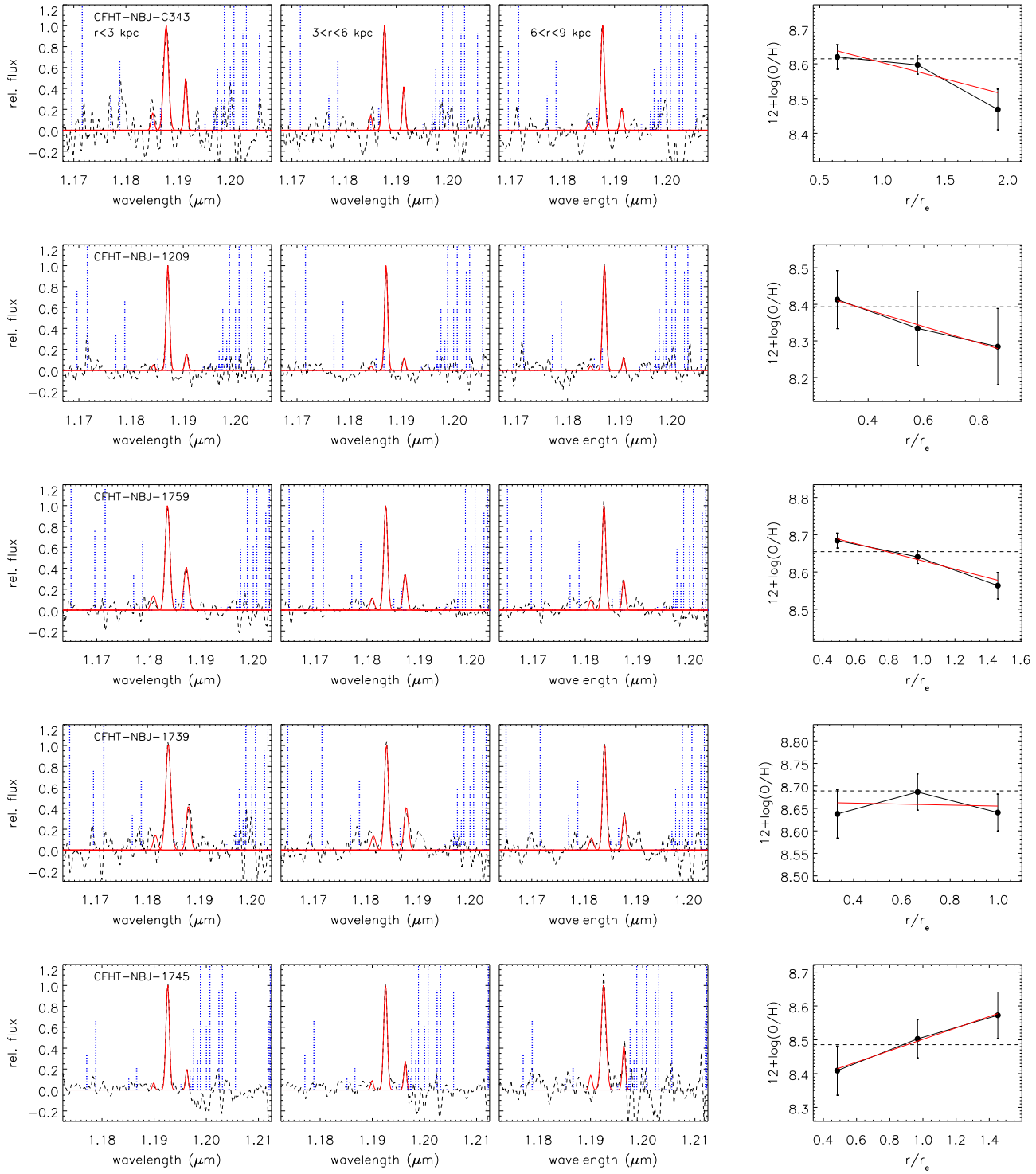

Figure 2. The metallicity gradients for five galaxies from the KMOS-HiZELS sample. Left-hand panel: these are the individual one-dimensional spectra from three concentric annuli at increasing galactocentric radius ($r < 3$, $3 < r < 6$, $6 < r < 9$ kpc). The red lines are fits to the Hα and [N II] emission lines. The dotted blue lines represent the location and relative flux of the sky emission. Right-hand panel: the metallicity derived from the ratio of [N II]/Hα plotted against galactocentric radius. The red line is a fit to the data points. The horizontal dashed line represents global metallicity value for the galaxy measured in a 1.2 arcsec diameter aperture.

significant outliers with metallicity gradients of $\sim -0.25\,\mathrm{dex\,kpc^{-1}}$ and sSFR $\sim 3 \times 10^{-8}$ and $\sim 5 \times 10^{-9}\,\mathrm{yr^{-1}}$.

For comparison with local galaxies, we include data points inferred from Rupke et al. (2010b) who study a sample of normal and merging star-forming galaxies in the local Universe. We derive SFRs for the Rupke et al. (2010b) sample by using their tabulated far-infrared luminosities, assuming Kennicutt (1998) and note that the majority of the mergers have $L_{\mathrm{IR}} \gtrsim 10^{10.5}\,\mathrm{L_\odot}$, with three

Table 2. The metallicity gradients for the 20 KMOS-HiZELS galaxies where it was possible to measure them.

Galaxy	$\frac{\Delta Z}{\Delta r}$ (dex kpc^{-1})	log (sSFR) (yr^{-1})
CFHT-NBJ-C339	0.004 ± 0.012	−9.6
CFHT-NBJ-C343	−0.020 ± 0.011	−9.9
CFHT-NBJ-956	−0.059 ± 0.015	−9.4
CFHT-NBJ-1209	−0.022 ± 0.022	−8.7
CFHT-NBJ-1709	0.007 ± 0.012	−10.0
CFHT-NBJ-1739	−0.001 ± 0.011	−9.7
CFHT-NBJ-1740	0.016 ± 0.010	−9.5
CFHT-NBJ-1745	0.025 ± 0.017	−9.0
CFHT-NBJ-1759	−0.018 ± 0.006	−9.3
CFHT-NBJ-1774	0.013 ± 0.012	−9.1
CFHT-NBJ-1787	0.007 ± 0.008	−9.7
CFHT-NBJ-1789	0.000 ± 0.007	−9.7
CFHT-NBJ-1790	0.032 ± 0.012	−9.2
CFHT-NBJ-1793	0.012 ± 0.009	−9.3
CFHT-NBJ-1795	−0.063 ± 0.019	−8.9
CFHT-NBJ-2044	−0.020 ± 0.008	−9.9
CFHT-NBJ-2048	0.073 ± 0.020	−8.2
VVDS-503	−0.010 ± 0.015	−8.6
VVDS-588	−0.031 ± 0.013	−9.6
VVDS-888	0.020 ± 0.014	−9.0

galaxies being luminous infrared galaxies (LIRGs, $L_{\rm IR} \gtrsim 10^{11}\,{\rm L}_{\odot}$). The majority of the non-mergers have $L_{\rm IR} \lesssim 10^{10}\,{\rm L}_{\odot}$. We derive stellar masses for their galaxies using their tabulated absolute K-band magnitudes, assuming an underlying simple stellar population model from Bruzual & Charlot (2003) that has a solar metallicity and was formed at $z = 1$ (i.e. ∼8 Gyr old). If we include the $z \sim 0$ Rupke et al. (2010b) sample in the sSFR, metallicity gradient fit, then the significance of the trend increases with the parameters becoming $c = 0.023 \pm 0.004$ and $d = 0.20 \pm 0.05$ (i.e. the slope is 5.8σ from being flat). As stated above, the effect of any unseen, low-level AGN activity would act to steepen the negative metallicity gradients but flattening the positive ones. This would therefore not affect the general trend of our result. We discuss the theoretical implications of the relationship between sSFR and metallicity gradient in Section 4. We also note that if we include the Rupke et al. (2010b) sample in the metallicity gradient mass fit, then the significance of that trend increases to only 2.7σ from a flat relation.

Finally, the average sSFR of the main sequence of typical star-forming galaxies increases with redshift (Elbaz et al. 2011; Sobral et al. 2014). Galaxies above this main sequence at a given redshift are often classed as 'starbursts', i.e. those that are most vigorously forming stars at that epoch. This means that a galaxy classed as a starburst at low redshift will have the same sSFR as the typical main-sequence galaxies at higher redshift. To account for this evolution, in order to compare main sequence galaxies to starbursts across all redshifts, we normalize the sSFR of the galaxies in Fig. 3 by the average sSFR of the main sequence at their redshift (using Elbaz et al. 2011). In Fig. 4, we plot this epoch normalized sSFR ($\rm sSFR_{EN} = sSFR/\langle sSFR(\mathit{z})\rangle$, cf. epoch normalized SFR; Stott et al. 2013a) against metallicity gradient. A similar trend to that in Fig. 3 is found, with the fit $\frac{\Delta Z}{\Delta r} = e\,\log(\rm sSFR_{EN}) + \mathit{f}$ returning a slope of $e = 0.028 \pm 0.007$ ($f = -0.02 \pm 0.01$). The galaxies on the main sequence are found to have an average metallicity gradient of -0.020 ± 0.004 while those in the starburst region have an average of 0.004 ± 0.006, a difference of 3.1σ. We note from Stott et al. (2013a) that galaxies on the main sequence at any redshift have a low major merger fraction (∼10 per cent) whereas those in the starburst region may have a merger fraction of ∼50 per cent. Environmental classifications for isolated and potentially interacting galaxies exist for the Queyrel et al. (2012) sample (see Epinat et al. 2012). From this, we find that the interacting galaxies do have a higher biweight average metallicity gradient of 0.028 ± 0.010 dex kpc^{-1} than the isolated galaxies, which have an average gradient of 0.003 ± 0.008 dex kpc^{-1}, but this is only an $\sim 2\sigma$ difference. We note that this difference is reduced to $\sim 1\sigma$ if we include the $K_{\rm Tot} > 0.5$ defined mergers from KMOS-HiZELS and Swinbank et al. (2012). We discuss the implications of the $\rm sSFR_{EN}$ and merging for the metallicity gradients in Section 4.

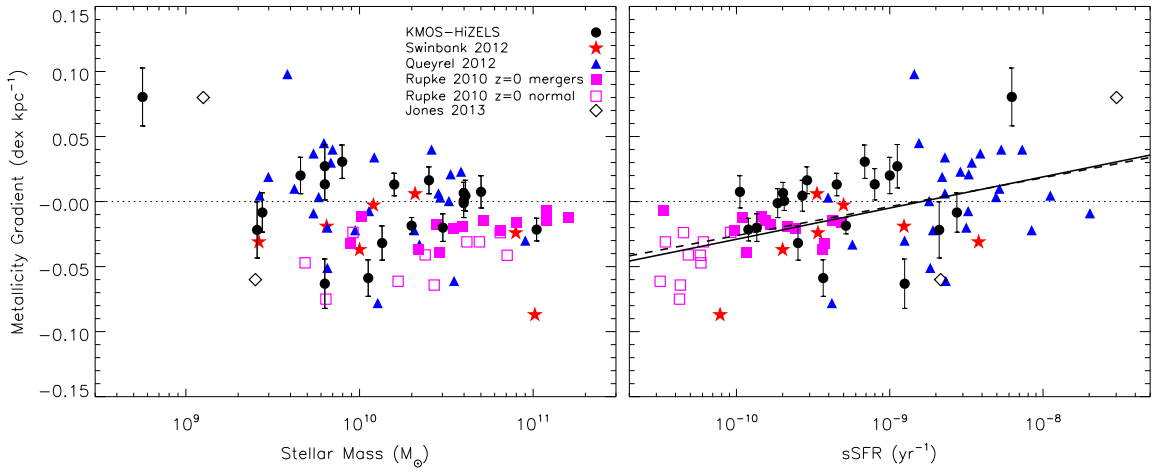

Figure 3. Left: the metallicity gradient plotted against stellar mass for the KMOS-HiZELS sample. We include the high-redshift samples of Swinbank et al. (2012) and Queyrel et al. (2012), and the local samples of normal and merging systems from Rupke et al. (2010b). We also plot two galaxies from the lensing sample of Jones et al. (2013). Right: the metallicity gradient plotted against sSFR for the same samples. The solid line is a fit to the combined data of KMOS-HiZELS, Swinbank et al. (2012), Queyrel et al. (2012) and Rupke et al. (2010b), which demonstrates that galaxies with higher sSFR tend to have more positive metallicity gradients. The dashed line is a fit to the high-redshift galaxies only, i.e. without the Rupke et al. (2010b) samples.

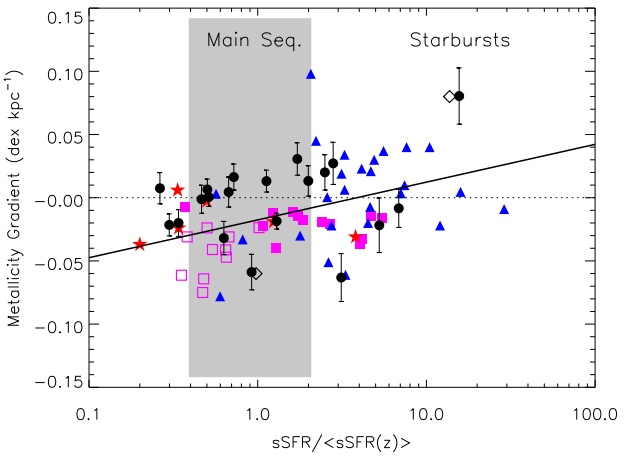

Figure 4. The metallicity gradient plotted against epoch normalized sSFR ($sSFR_{EN}$ = sSFR/⟨sSFR(z)⟩) for the samples shown in Fig. 3. The grey region represents the main sequence ($sSFR_{EN} = 1$) with a factor of 2 in $sSFR_{EN}$ either side. The starburst galaxies populate the region with $sSFR_{EN} > 2$. The solid line is a fit to the combined data of KMOS-HiZELS, Swinbank et al. (2012), Queyrel et al. (2012) and Rupke et al. (2010b), which demonstrates that the starbursts tend to have more positive metallicity gradients.

3.2.1 *The effect of atmospheric seeing and inclination*

The metallicity gradient will be affected by the seeing. We measure the metallicity in elliptical annuli and expect galaxies with the largest ellipticities, due to their large angles of inclination, to be affected more than those that are face-on. This is because the annuli are closer together in the minor axis direction and are separated by less than the half width at half maxima (HWHM) of the seeing disc.

We test the combined effect of seeing and inclination by performing a simulation of 1000 discs with random input metallicity gradients in the range $-0.2 < \frac{\Delta Z}{\Delta r} < 0.2$ and random inclination angles of $0^\circ < i < 90^\circ$. These discs are then smoothed with a Gaussian kernel, with an FWHM the same as the observed atmospheric seeing (0.7 arcsec). The results of this test are that for a face-on disc, the metallicity gradient we observe in 0.7 arcsec seeing will be ∼80 per cent of its true value. When we consider the inclination angle as well, the observed metallicity gradient at the median inclination of the KMOS-HiZELS sample (50°) will only be 70 per cent of its intrinsic value. The most extreme correction to our sample comes for the galaxy with the largest positive gradient (CFHT-NBJ-2048, $\frac{\Delta Z}{\Delta r} = 0.07$, $i = 80^\circ$) for which we may only be observing 30 per cent of its true value. For all other galaxies in KMOS-HiZELS, we observe at least 50 per cent of their intrinsic metallicity gradient.

We note that the flattening effect we see is less dramatic than that seen by Yuan et al. (2013, see also Mast et al. 2014), who find that the measured value of the metallicity gradient is only ∼10–20 per cent of its true value for a simulation of a degraded face-on disc, in similar seeing conditions to those seen here. The reason for this is that our annuli are evenly spaced such that the outer radius is not contaminated by higher metallicity material close to the galaxy core. Yuan et al. (2013) use the annular radii: $\lesssim$1.5, ∼1.5–3.5 and ∼3.5–9 kpc (cf. our annuli <3, 3–6 and 6–9 kpc). Also, the effect of the seeing on their galaxy is more significant as it is at $z = 1.49$, where the FWHM of 0.7 arcsec corresponds to 6 kpc, whereas at $z = 0.8$ this is 5 kpc.

The local samples of Rupke et al. (2010b) and the high-resolution, adaptive optics observed samples of Swinbank et al. (2012) and Jones et al. (2013) will be significantly less affected by seeing. However, the Queyrel et al. (2012) sample will be affected in a similar way to our own. We therefore perform a seeing correction to our data using the individual inclination angle values and one to the Queyrel et al. (2012) sample, assuming the average inclination of our sample for all of their galaxies. We refit the trend between sSFR and metallicity gradient using the seeing-corrected KMOS-HiZELS and Queyrel et al. (2012) data and find that the parameters from Section 3.2 become $c = 0.026 \pm 0.006$ and $d = 0.23 \pm 0.06$. These parameters represent an increased slope as expected but agree with the previous values within 1σ. We therefore conclude that removing the effect of the atmospheric seeing only acts to strengthen our result.

4 DISCUSSION

Simulations of the evolution of disc galaxies that predict inside-out growth tend to have initially steep negative abundance gradients which then flatten at later times (e.g. Marcon-Uchida et al. 2010; Stinson et al. 2010; Gibson et al. 2013). Alternatively, flattened and positive gradients have been interpreted as suggesting an inflow of metal-poor gas to their central regions. This may be triggered by either mergers (Rupke et al. 2010a) or cold flows (Kereš et al. 2005; Dekel et al. 2009; Cresci et al. 2010). The significant correlation we find between metallicity gradient and sSFR is consistent with this picture, as galaxies with an increased sSFR are thought to be fuelled by gas flowing towards their centres, caused by either merging or efficient accretion.

Our results may explain why there are competing claims on how the gas phase metallicity gradient evolves with redshift (see Fig. 5) with some claiming positive gradients at high z (Cresci et al. 2010; Queyrel et al. 2012) and others negative (e.g. Swinbank et al. 2012) as it appears that this may just be driven by the different sSFRs of the observed samples. For example, the median $\log(\mathrm{sSFR\ yr^{-1}}) = -8.5$ for Queyrel et al. (2012), who find a median metallicity gradient of $+0.005$ dex kpc^{-1}, and the median $\log(\mathrm{sSFR\ yr^{-1}}) = -9.5$ for Swinbank et al. (2012), who find an median metallicity gradient of -0.024 dex kpc^{-1}. It also explains the difference in slope between the 'normal' star-forming galaxies and merging LIRG-like systems, as seen by Rupke et al. (2010b) in the local Universe. From a galaxy evolution perspective, our findings mean that a galaxy's sSFR is governed by the amount of (typically metal poor) gas that can be funnelled into its core, triggered either by merging or efficient accretion.

This picture is also in agreement with the observed fundamental metallicity relation (FMR; Lara-López et al. 2010; Mannucci et al. 2010; Stott et al. 2013b) in which galaxies at a fixed stellar mass are found to be more metal poor with increasing SFR. In fact, as measurements of the FMR tend to use spectroscopy of the bright inner regions of the galaxy due to the limited size of spectroscopic slits and fibres (e.g. SDSS, Mannucci et al. 2010; FMOS, Stott et al. 2013b), then the relation between sSFR and metallicity gradient presented in this paper may help to explain the FMR. To quantify this, we consider two galaxies, both of mass $1 \times 10^{10}\,\mathrm{M_\odot}$, with SFR = 1 and $50\,\mathrm{M_\odot\ yr^{-1}}$, respectively. If we assume that both galaxies have a solar metallicity (8.66 dex) at a galactocentric radius of 5 kpc, then we can use the relationship between sSFR and metallicity gradient to calculate their central metallicities. These are predicted to be 8.8 and 8.6 dex, respectively, i.e. a difference of 0.2 dex. Using the FMR equation of Mannucci et al. (2010), the

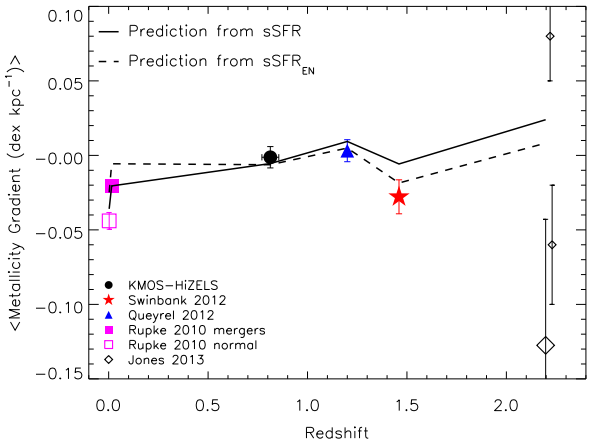

Figure 5. The average metallicity gradient plotted against average redshift for the samples used in Fig. 3. Our KMOS-HiZELS and the Queyrel et al. (2012) results indicate that the metallicity gradient becomes more positive with redshift whereas the Swinbank et al. (2012) data suggest no evolution. Finally, the Jones et al. (2013) average, represented by the large open diamond, would suggest that the slope becomes more negative. We note that there are only four independent Jones et al. (2013) galaxies, and therefore the two galaxies with metallicity gradients of -0.25 dex kpc^{-1} and sSFR $\sim 3 \times 10^{-8}$ and $\sim 5 \times {}^{-9}$ yr^{-1} (which were outliers to the fit in Fig. 3) lower the average significantly. However, the two smaller diamonds represent the other two galaxies in the Jones et al. (2013) sample that do follow our trend. The solid and dashed lines are the prediction due to the trends between sSFR and sSFR$_{EN}$ with metallicity gradient, respectively, as shown in Figs 3 and 4. They both successfully explain the competing claims for how the metallicity gradient appears to evolve with redshift.

predicted difference in metallicity due to the difference in SFR at fixed mass is 0.25 dex, which is in good agreement.

We now discuss whether we can determine if mergers or accretion are responsible for the trend between metallicity gradient and sSFR. The average sSFR of the main sequence of typical star-forming galaxies increases with redshift (Elbaz et al. 2011). In the redshift range $z \leq 2.2$, the major merger fraction on the main sequence is found to be constant at $\sim$10 per cent (Stott et al. 2013a), which suggests that the reason for the increase in sSFR is either secular processes, such as cold flows, or minor merging. However, the major merger fraction is found to increase with sSFR at a given redshift (i.e. relative to the star-forming main sequence of that epoch), such that $\sim$50 per cent of starbursts at any epoch are major mergers (Stott et al. 2013a). When these two observations are taken in concert, it means that although a low-redshift starburst galaxy is likely to be driven by a merger, it will have the same sSFR as the non-merging main-sequence population at high redshift. Both the secular sSFR evolution of the main sequence and the increase in sSFR at a given epoch due to merging could provide a mechanism for forcing metal-poor gas towards the centres of star-forming galaxies. It is therefore difficult to separate out the effects of merging and secular processes as the cause for the trend in metallicity gradient with sSFR shown in Fig. 3. To account for this, we normalize the sSFR to the average of the main sequence at the galaxies' redshift and plot this against metallicity gradient in Fig. 4. From this analysis, we find that the average metallicity gradient of the main-sequence galaxies is significantly more negative than the starbursts. This suggests that merging may play a significant role in driving the metallicity gradient to more positive values. In Fig. 5, we include a prediction for the metallicity gradient of the samples with redshift based on the trend with the epoch normalized sSFR (sSFR$_{EN}$) from Section 3.2 and Fig. 4. However, we note that the evidence for more positive metallicity gradients in galaxies with dynamical or visual indicators of merging is of low statistical significance ($\sim 1\sigma$–2σ). Therefore, secular processes, which increase in efficiency with redshift, may still be important.

5 SUMMARY

We have observed a sample of 39 typical star-forming galaxies at $z \sim 1$ with KMOS to investigate their dynamics and metallicity gradients. From these data, we conclude as follows.

(i) The majority of the KMOS-HiZELS sample of $z \sim 1$ star-forming galaxies show disc-like rotation.

(ii) The metallicity gradients of the galaxies are generally consistent with being either flat or negative (higher metallicity in the galaxy core relative to outer regions).

(iii) There is a trend between sSFR and metallicity gradient, in that galaxies with a higher sSFR tend to have a relatively metal poor centre.

(iv) When we account for the average sSFR of the star-forming main sequence, it seems that the starbursts have significantly more positive metallicity gradients than typical galaxies.

The trend between sSFR and metallicity gradient suggests that the funnelling of metal-poor gas into the centres of galaxies, triggered via either merging or efficient accretion, is the driver of high sSFRs. In fact, merging may play a significant role as it is the starburst galaxies at all epochs, which have the more positive metallicity gradients. The trend with sSFR helps to explain the conflicting observational claims for how the metallicity gradient of galaxies evolves with redshift. Our results may also explain the FMR in which there is observed to be a negative correlation between metallicity and SFR at fixed galaxy mass.

ACKNOWLEDGEMENTS

First, we acknowledge the referee for their comments, which have improved the clarity of this paper. JPS and IRS acknowledge support from STFC (ST/I001573/1). IRS also acknowledges support from the ERC Advanced Investigator programme DUSTYGAL and a Royal Society/Wolfson Merit Award. DS acknowledges financial support from NWO through a Veni fellowship and from FCT through the award of an FCT-IF starting grant. PNB acknowledges STFC for financial support.

REFERENCES

Alloin D., Collin-Souffrin S., Joly M., Vigroux L., 1979, A&A, 78, 200
Asplund M., Grevesse N., Sauval A. J., Allende Prieto C., Kiselman D., 2004, A&A, 417, 751
Baldwin J. A., Phillips M. M., Terlevich R., 1981, PASP, 93, 5
Bertin E., Arnouts S., 1996, A&AS, 117, 393
Bresolin F., Kennicutt R. C., Ryan-Weber E., 2012, ApJ, 750, 122
Bruzual G., Charlot S., 2003, MNRAS, 344, 1000
Chabrier G., 2003, PASP, 115, 763
Charbonneau P., 1995, ApJS, 101, 309
Courteau S., 1997, AJ, 114, 2402
Cresci G. et al., 2009, ApJ, 697, 115
Cresci G., Mannucci F., Maiolino R., Marconi A., Gnerucci A., Magrini L., 2010, Nature, 467, 811
Davies R. I., 2007, MNRAS, 375, 1099
Davies R. I. et al., 2013, A&A, 558, A56

Dekel A., Sari R., Ceverino D., 2009, ApJ, 703, 785
Denicoló G., Terlevich R., Terlevich E., 2002, MNRAS, 330, 69
Elbaz D. et al., 2011, A&A, 533, A119
Epinat B. et al., 2012, A&A, 539, A92
Erb D. K., Shapley A. E., Pettini M., Steidel C. C., Reddy N. A., Adelberger K. L., 2006, ApJ, 644, 813
Garnett D. R., Shields G. A., Skillman E. D., Sagan S. P., Dufour R. J., 1997, ApJ, 489, 63
Geach J. E., Smail I., Best P. N., Kurk J., Casali M., Ivison R. J., Coppin K., 2008, MNRAS, 388, 1473
Gibson B. K., Pilkington K., Brook C. B., Stinson G. S., Bailin J., 2013, A&A, 554, A47
Gonçalves T. S. et al., 2010, ApJ, 724, 1373
Henry R. B. C., Worthey G., 1999, PASP, 111, 919
Jones T., Ellis R. S., Richard J., Jullo E., 2013, ApJ, 765, 48
Karim A. et al., 2011, ApJ, 730, 61
Kennicutt R. C., Jr, 1998, ARA&A, 36, 189
Kereš D., Katz N., Weinberg D. H., Davé R., 2005, MNRAS, 363, 2
Kewley L. J., Dopita M. A., 2002, ApJS, 142, 35
Kewley L. J., Ellison S. L., 2008, ApJ, 681, 1183
Kewley L. J., Dopita M. A., Sutherland R. S., Heisler C. A., Trevena J., 2001, ApJ, 556, 121
Krajnović D., Cappellari M., de Zeeuw P. T., Copin Y., 2006, MNRAS, 366, 787
Lamareille F. et al., 2009, A&A, 495, 53
Lara-López M. A. et al., 2010, A&A, 521, L53
Le Fèvre O. et al., 2005, A&A, 439, 845
McCall M. L., Rybski P. M., Shields G. A., 1985, ApJS, 57, 1
Maiolino R. et al., 2008, A&A, 488, 463
Mannucci F., Cresci G., Maiolino R., Marconi A., Gnerucci A., 2010, MNRAS, 408, 2115
Marcon-Uchida M. M., Matteucci F., Costa R. D. D., 2010, A&A, 520, A35
Mast D. et al., 2014, A&A, 561, A129
Matthee J. J. A. et al., 2014, MNRAS, 440, 2375
Newman S. F. et al., 2014, ApJ, 781, 21
Noeske K. G. et al., 2007, ApJ, 660, L43
Peng C. Y., Ho L. C., Impey C. D., Rix H.-W., 2002, AJ, 124, 266
Pérez-Montero E. et al., 2009, A&A, 495, 73
Pettini M., Pagel B. E. J., 2004, MNRAS, 348, L59
Puget P. et al., 2004, in Moorwood A. F. M., Iye M., eds, Proc. SPIE Conf. Ser. Vol. 5492, Ground-Based Instrumentation for Astronomy. SPIE, Bellingham, p. 978
Queyrel J. et al., 2012, A&A, 539, A93
Rich J. A., Dopita M. A., Kewley L. J., Rupke D. S. N., 2010, ApJ, 721, 505
Rupke D. S. N., Kewley L. J., Barnes J. E., 2010a, ApJ, 710, L156
Rupke D. S. N., Kewley L. J., Chien L.-H., 2010b, ApJ, 723, 1255
Salpeter E. E., 1955, ApJ, 121, 161
Sánchez S. F. et al., 2012, A&A, 546, A2
Sánchez S. F. et al., 2014, A&A, 563, A49
Savaglio S. et al., 2005, ApJ, 635, 260
Searle L., 1971, ApJ, 168, 327
Shapiro K. L. et al., 2008, ApJ, 682, 231
Sharples R. et al., 2013, The Messenger, 151, 21
Shields G. A., 1974, ApJ, 193, 335
Sobral D. et al., 2009, MNRAS, 398, 75
Sobral D., Best P. N., Smail I., Geach J. E., Cirasuolo M., Garn T., Dalton G. B., 2011, MNRAS, 411, 675
Sobral D., Best P. N., Matsuda Y., Smail I., Geach J. E., Cirasuolo M., 2012, MNRAS, 420, 1926
Sobral D., Smail I., Best P. N., Geach J. E., Matsuda Y., Stott J. P., Cirasuolo M., Kurk J., 2013a, MNRAS, 428, 1128
Sobral D. et al., 2013b, ApJ, 779, 139
Sobral D., Best P. N., Smail I., Mobasher B., Stott J., Nisbet D., 2014, MNRAS, 437, 3516
Stinson G. S., Bailin J., Couchman H., Wadsley J., Shen S., Nickerson S., Brook C., Quinn T., 2010, MNRAS, 408, 812
Stott J. P., Sobral D., Smail I., Bower R., Best P. N., Geach J. E., 2013a, MNRAS, 430, 1158
Stott J. P. et al., 2013b, MNRAS, 436, 1130
Swinbank A. M., Sobral D., Smail I., Geach J. E., Best P. N., McCarthy I. G., Crain R. A., Theuns T., 2012, MNRAS, 426, 935
Tremonti C. A. et al., 2004, ApJ, 613, 898
van Zee L., Salzer J. J., Haynes M. P., O'Donoghue A. A., Balonek T. J., 1998, AJ, 116, 2805
Vila-Costas M. B., Edmunds M. G., 1992, MNRAS, 259, 121
Wright S. A., Larkin J. E., Graham J. R., Ma C.-P., 2010, ApJ, 711, 1291
Yabe K. et al., 2012, PASJ, 64, 60
Yuan T.-T., Kewley L. J., Rich J., 2013, ApJ, 767, 106
Zahid H. J., Geller M. J., Kewley L. J., Hwang H. S., Fabricant D. G., Kurtz M. J., 2013, ApJ, 771, L19
Zaritsky D., Kennicutt R. C., Jr, Huchra J. P., 1994, ApJ, 420, 87

This paper has been typeset from a TEX/LATEX file prepared by the author.